The Response of Westerly Jets to Thermal Driving in a Primitive Equation Model

SEOK-WOO SON AND SUKYOUNG LEE

Department of Meteorology, The Pennsylvania State University, University Park, Pennsylvania

(Manuscript received 7 September 2004, in final form 7 April 2005)

ABSTRACT

The structure of westerly jets in a statistically steady state is investigated with both dry and moist models on the sphere. The dry model is forced with an idealized radiative equilibrium temperature profile that consists of a global-scale base profile plus both localized tropical heating and high-latitude cooling. The tropical heating controls the intensity of the subtropical jet, while the high-latitude cooling modulates the meridional width of the extratropical baroclinic zone.

The jet structure is analyzed with a large number of dry model runs in which the tropical heating and high-latitude cooling rates are systematically varied. This parameter study shows that, in a regime with weak tropical heating and strong high-latitude cooling, the polar-front jet separates itself from the subtropical jet, forming a double-jet state. In contrast, if the tropical heating rate is greater than a certain value, a strong single jet emerges, indicating that the presence of one or two jets in a statistically steady state is dependent upon the relative values of both the tropical heating and the baroclinic zone width.

A set of moist model runs is examined in which the moisture content is systematically varied. For a relatively small moisture content, the circulation prefers a double-jet state. However, for a moisture content that is greater than a certain threshold value, the two jets collapse into a single jet. With the aid of the aforementioned dry model results, an explanation for this nonlinear response exhibited by the moist model is provided. Based on the results of the dry and moist model calculations, this paper discusses various physical interpretations of the circulation responses to global warming presented in the literature.

1. Introduction

There are two types of tropospheric jets: the subtropical jet (STJ) that is driven by angular momentum transfer from the deep Tropics through the Hadley circulation (Schneider 1977; Held and Hou 1980; Lindzen and Hou 1988) and the eddy-driven or polar-front jet (PFJ) that is generated by midlatitude baroclinic eddies (James 1994). As such, while the two jets are not dynamically independent of each other, the STJ would exist in an eddy-free state, but the PFJ owes its existence to the eddies.

Lee and Kim (2003, hereafter LK03) recently examined the impact of the STJ on the development of the PFJ. Using an initial-value approach, they found that the PFJ develops at about the same latitude as the STJ when the STJ is sufficiently strong. This produces a single jet that combines the characteristics of both a STJ and PFJ. If the STJ is not sufficiently strong, the most favorable region for baroclinic wave growth lies 20°–30° poleward of the STJ, driving the PFJ at those higher latitudes. The result is a well-defined double-jet state with distinct STJ and PFJ. As discussed by LK03, while these results bear potentially important implications for a better understanding of both midlatitude storm track dynamics (see also Nakamura et al. 2004) and for the North Atlantic Oscillation teleconnection pattern, there are severe limitations for applying the results of the initial-value calculations to the real atmosphere.

The goal of this study is to examine the extent to which the results from the initial value problem of LK03 hold for statistically steady states. As will be justified in section 2, the approach to be taken is a parameter study of the jet structure, where the primary parameters to be varied are the tropical heating and high-latitude cooling rates. Keeping an application to the real atmosphere in mind, the parameter study is further extended to the moist atmosphere. With the help of moist model runs and from the results of our parameter study, we also aim to improve our understanding of the general circulation response to global warming.

Corresponding author address: Seok-Woo Son, Dept. of Meteorology, 503 Walker Building, The Pennsylvania State University, University Park, PA 16802.
E-mail: sus141@psu.edu

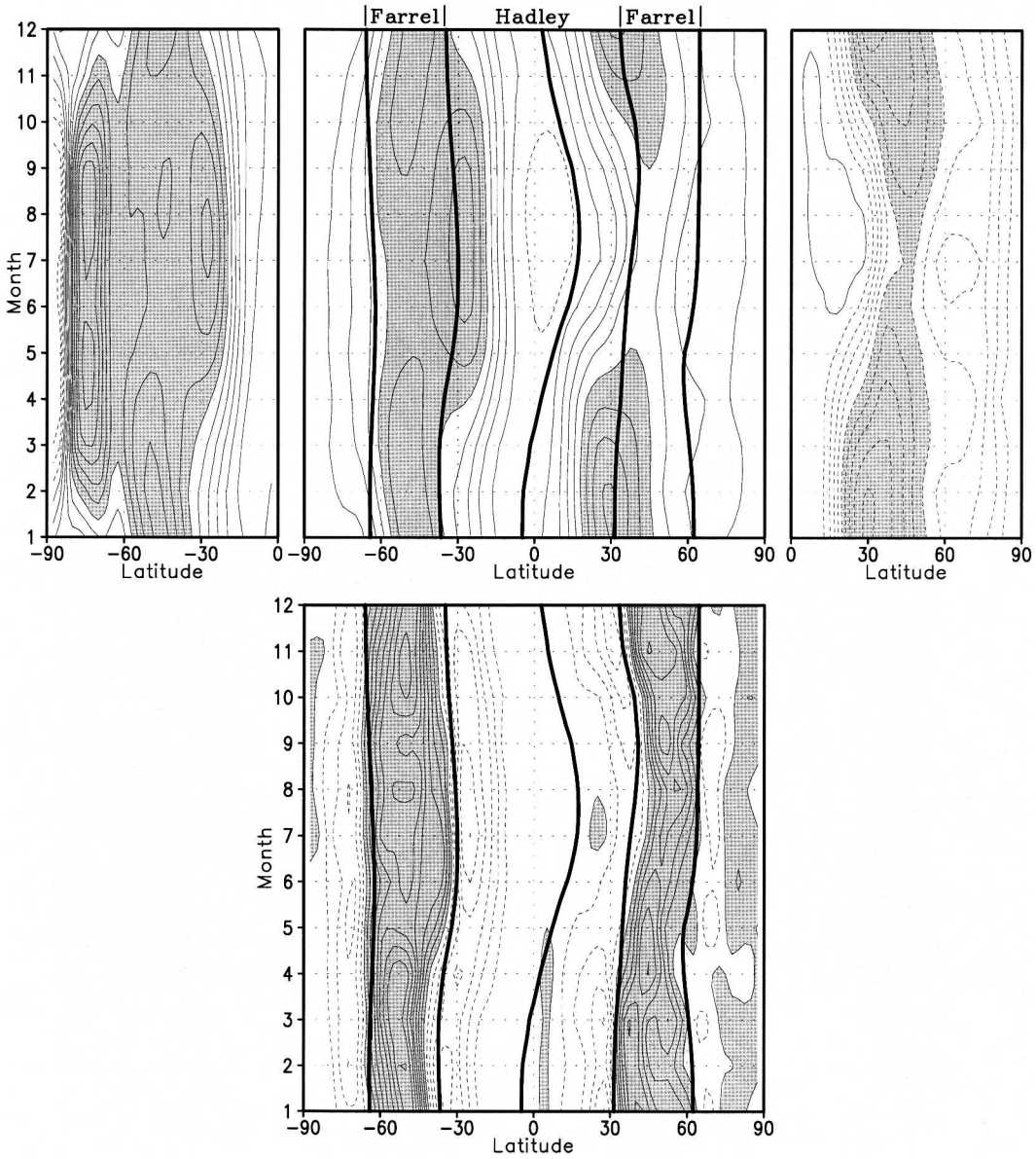

FIG. 1. (top center) Monthly mean zonal-mean fields: 300-hPa $[\overline{u}]$, (bottom center) 300-hPa eddy momentum flux convergence, and (top left) meridional gradient of 700-hPa potential temperature in the SH and (top right) in the NH. The shadings in the center panels denote zonal wind speed greater than 20 m s^{-1}, and positive eddy momentum flux convergence. The thick lines in the center panels are zero lines of the zonal-mean surface meridional wind. The shading in the side panels is above 5×10^{-6} K m^{-1} in absolute value.

This paper is organized as follows. The experiment strategy and numerical model are described in section 2. The results of dry and moist model runs are described in sections 3 and 4, respectively. Section 5 compares the results of the statistically steady-state calculations with those of the initial value problem of LK03. The summary is presented in section 6. The implications of our results for the atmosphere and for the climate response to global warming are discussed in section 7.

2. Experiment design

a. Rationale for the key parameters

Both dry and moist models are forced with an idealized, global-scale radiative equilibrium temperature profile [the function F in (1), referred to as the base profile]. For the dry model, we also add localized tropical heating and high-latitude cooling to the base profile [see (1)]. The tropical heating controls the intensity of

the STJ, while the high-latitude cooling is designed to modulate the meridional width of the extratropical baroclinic zone. The latter choice was based upon the expectation that a broader baroclinic zone, by providing more room for the development of a PFJ, is more conducive to generating a double-jet state (cf. Panetta 1993; Lee 1997).

The observations are consistent with the above conjectures, as can be seen from Fig. 1, which shows the temporal evolution of the monthly mean zonal-mean 300-hPa zonal wind, 300-hPa eddy momentum flux convergence, and 700-hPa potential temperature gradient. The thick solid lines in the center panels are the zero lines of zonal-mean surface meridional wind $[v]_{\text{sfc}}$, which show the approximate locations of the Hadley and Ferrel cell boundaries. These mean fields are derived from National Centers for Environmental Prediction–National Center for Atmospheric Research (NCEP–NCAR) reanalysis data.

As can be inferred from the collocation of the jets with the corresponding poleward boundary of the Hadley cells, the wintertime jets in both hemispheres are essentially STJs. However, during equinoctial conditions, unlike for the Northern Hemisphere (NH) jet, which is still predominately a STJ, the Southern Hemisphere (SH) wind field shows characteristics of both a STJ and a PFJ. The latter can be identified as such because it is latitudinally collocated with both the eddy momentum flux convergence (see bottom-center panel) and the Ferrel cell.[1] These SH double-jet states are apparently associated with a relatively broad baroclinic zone, as can be inferred from the meridional temperature gradient (see the upper left panel). In the NH, the baroclinic zone is relatively narrow for all seasons. We note that in both hemispheres, the summer season jet is predominantly a PFJ because the Hadley cell in the summer hemisphere is very weak (Lindzen and Hou 1988), hence the STJ is essentially absent during that season.

b. Model

We use a global spectral model that is based on the dynamical core of the Geophysical Fluid Dynamics Laboratory (GFDL) general circulation model (GCM) (Gordon and Stern 1982). The dynamic core of the GFDL GCM was made available to us originally by Isaac Held of GFDL. We adopt an aquaplanet configuration with the lower boundary of the model being zonally symmetric. To keep the computational demand for the parameter study at a reasonable level, while resolving the eddies with an acceptable accuracy, the zonal resolution is truncated at wavenumber 15 while the meridional resolution is truncated at wavenumber 30 (R15/30 hereafter). For several selected cases, the results are compared with those from a calculation with a rhomboidal 30 (R30 hereafter) resolution. As will be shown later, the zonal-mean states from these two versions of the model are almost indistinguishable from each other. In the vertical, there are 10 equally spaced sigma levels that vary from 0.95 to 0.05. Again, for a few selected runs, the statistically steady states from this resolution were almost identical to those with 20 sigma levels. The steady state is calculated by averaging an 800-day integration after discarding the first 300 days. Data from both hemispheres are used to reduce sampling errors.

The above primitive equation (PE) model is driven by relaxing temperature toward a radiative equilibrium temperature profile T_e with a time scale τ_R (= 30 days);

$$\frac{T_e(\hat{h}, \hat{c}, \varphi, \sigma)}{T_0\sigma^{R/C_p}} = \begin{cases} \underbrace{\dfrac{\hat{h}}{\alpha}\cos^2\left(\dfrac{\pi\varphi}{2\varphi_h}\right)}_{\text{tropical heating}} + F(\Delta, \Upsilon, \varphi_h, \sigma) & \text{for} \quad 0^\circ \le \varphi \le \varphi_h \\ F(\Delta, \Upsilon, \varphi, \sigma) & \text{for} \quad \varphi_h < \varphi < \varphi_c, \\ \underbrace{\hat{c}\alpha\left\{\cos\varphi_c(2\cos\varphi - \cos\varphi_c) - 1 + \dfrac{\alpha}{3}\right\}}_{\text{high-latitude cooling}} + F(\Delta - \hat{c}, \Upsilon, \varphi, \sigma) & \text{for} \quad \varphi_c \le \varphi \le 90^\circ \end{cases} \tag{1}$$

where

$$F(\delta, \Upsilon, \varphi, \sigma) = 1 - \delta\left(\alpha\sin^2\varphi - \frac{1}{3}\right) - \Upsilon(0.8\ln\sigma + 0.5),$$

with δ being equal to either Δ or $\Delta - \hat{c}$. Here, T_e is normalized by $T_o\sigma^{R/C_p}$, where R, C_p, and T_o are the gas

[1] It has been shown theoretically (Schneider 1977; Held and Hou 1980) that the STJ must be located at the poleward end of the Hadley cell where $[v]_{\text{sfc}} = 0$. Similarly, because both the heat and vorticity fluxes of the baroclinic waves, which drive the PFJ, also induce the thermally indirect Ferrel cell, the PFJ must be centered between two zero $[v]_{\text{sfc}}$ lines that mark the boundaries of the Ferrel cell.

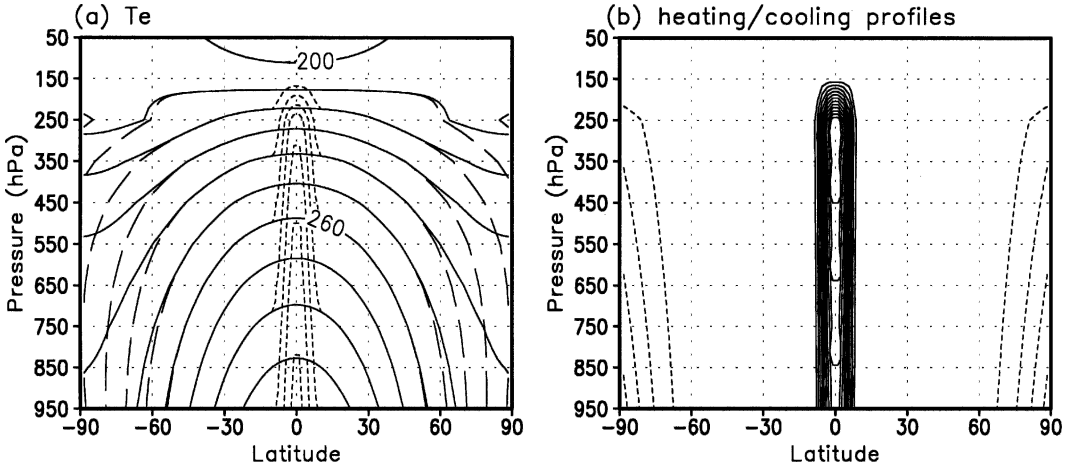

FIG. 2. (a) Profiles of T_e for ($\mathcal{H}$, $\mathcal{C}$) = (0.00, 0.00) K day^{-1} (solid), ($\mathcal{H}$, $\mathcal{C}$) = (0.00, 0.83) K day^{-1} (long dashed), and ($\mathcal{H}$, $\mathcal{C}$) = (1.67, 0.00) K day^{-1} (short dashed). (b) The T_e difference between the latter two cases. The contour intervals are (a) 10 K day^{-1} and (b) 5 K day^{-1}.

constant, the specific heat at constant pressure, and the reference temperature (= 300 K), respectively.

The base profile, F, is a function of δ, Υ, φ, and σ, which represent the meridional temperature gradient, the temperature lapse rate, latitude, and sigma level, respectively. This form for F is the same as that used by Held and Hou (1980) except for the presence of the parameter α, which is specified as being equal to $(1 + 2\sigma)/3$. The parameter α is introduced in this study both in order to reduce the meridional temperature gradient in the upper troposphere and to increase the high-latitude static stability. Figure 2a shows the base T_e profile (solid lines).

In (1), the terms for the additional tropical heating and high-latitude cooling are indicated with braces. These terms are applied at latitudes equatorward of φ_h ($\equiv 10°$) and poleward of φ_c ($\equiv 45°$), respectively. The amplitudes of these heating and cooling functions are controlled by the parameter $\hat{h}$ and $\hat{c}$, and their vertical structures are determined by α. The heating rate at the equator and cooling rate at the poles are equal to $\hat{h}T_o\sigma^{R/C_p}(\alpha\tau_R)^{-1}$ and $\hat{c}T_o\sigma^{R/C_p}\alpha(2\tau_R)^{-1}$, respectively. Since $\hat{h}$ and $\hat{c}$ are the only parameters that are varied in the experiments, hereafter, each experiment will be referred to by the surface values of the equatorial heating rate, $\mathcal{H}(\equiv \hat{h}T_o\tau_R^{-1})$, and the polar cooling rate, $\mathcal{C}(\equiv \hat{c}T_o(2\tau_R)^{-1})$. Note that $\sigma = \alpha = 1$ at the surface. Figure 2b shows examples of additional tropical heating and high-latitude cooling profiles.

The dissipation processes in the model are the same as those used by Kim and Lee (2001). Briefly, the model atmosphere is subject to a nonlinear surface drag with a time scale of about 1 day, to vertical diffusion with a coefficient $\nu = 0.5$ m^2 s^{-1}, and to scale selective eighth-order horizontal diffusion with a coefficient value of 8×10^{37} m^8 s^{-1}. It has been shown that the jet structure can be sensitive to parameterizations for both surface drag and diffusion (James and Gray 1986; Stephenson 1995; Robinson 1997). Therefore, while the main focus of this study is the effect of the tropical heating and high-latitude cooling on the jet structure, its sensitivity to the above parameterizations are also examined. Consistent with Robinson (1997), the location of the jets shifts poleward with decreasing surface friction. However, its sensitivity to the horizontal diffusion coefficient is found to be rather weak. For all runs, the initial perturbations take the form of a Gaussian distribution both in longitude and in latitude, thereby projecting onto all waves resolved by the model.

c. Base run

We briefly describe the zonal-mean structure of the base run for which ($\mathcal{H}$, $\mathcal{C}$) = (0.00, 0.00) K day^{-1}. Unless stated otherwise, for all model runs to be presented in this study, the values for ($T_o\Delta$, $T_o\Upsilon$) are fixed at (60, 37.5) K. The T_e profile for the base run is illustrated in Fig. 2a.

Figure 3a shows $[\overline{u}]$ for the base run, where the brackets denote the zonal mean, the overbar the time mean, and u is the zonal wind. As stated earlier, this wind field is almost identical to that from a separate simulation with R30 resolution (Fig. 3b), ensuring that the additional truncation in the zonal direction is essentially inconsequential. Superimposed on Figs. 3a and 3b are, respectively, the mean meridional mass streamfunction and the eddy momentum flux convergence of the base run. As can be seen in Fig. 3a, at the poleward

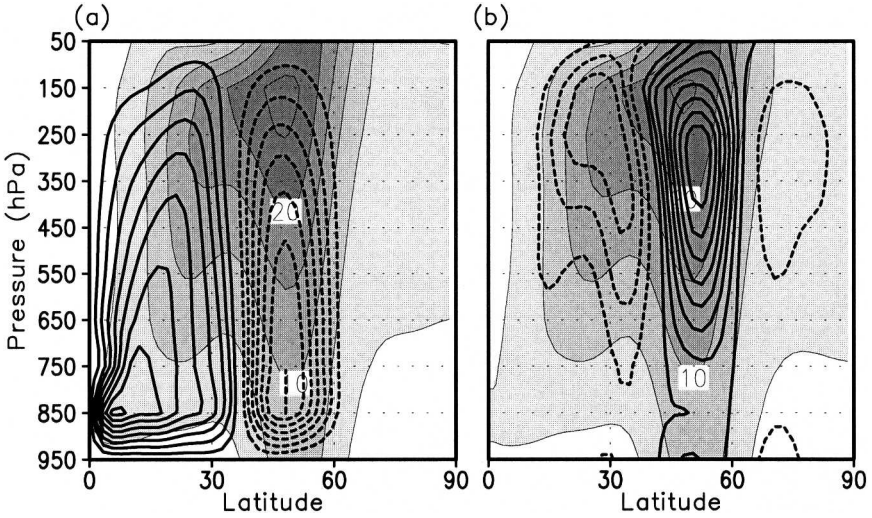

FIG. 3. Statistically steady-state zonal-mean fields of the base run: (a) mass streamfunction and (b) eddy momentum flux convergence. The contour intervals are (a) 3×10^9 kg s^{-1} and (b) 2×10^{-6} m s^{-2}. The zero lines are omitted. The superimposed shading in (a) is $[\overline{u}]$ of the base run. For comparison with the base run, $[\overline{u}]$ from the model with a R30 resolution is displayed in (b). In both (a) and (b), only westerlies are shaded with a 5 m s^{-1} interval.

boundary of the Hadley cell (~30°), there is an indication of a weak STJ in the vicinity of the 350-hPa level. Figure 3b shows that the primary jet centered at around 45° is a PFJ, as it is characterized by a deep vertical structure, and is collocated with the maximum eddy momentum flux convergence.

d. Moist run

To construct a moist model consistent with the dry model described above, we adopt an approach similar to that used by Hoskins (1983). In the moist version of the model, the flow is still relaxed toward the base equilibrium temperature profile, but with the extra heating and cooling terms being set to zero; that is, $(\mathcal{H}, C) = (0.00, 0.00)$ K day^{-1}. The effect of moisture is parameterized by the moist-convective adjustment and large-scale condensation of Manabe et al. (1965). Further details are described in the appendix.

3. Effect of tropical heating ($\mathcal{H}$) versus high-latitude cooling (C)

Based on the structure of $[\overline{u}]$, we define the jet structures as follows: a double jet is characterized by a minimum wind speed at 250 hPa that is located between the STJ and the PFJ, with a value less than U_c; a single jet has one maximum in $[\overline{u}]$ at 450 hPa; an intermediate jet satisfies neither of the above two conditions. The critical wind speed U_c is defined as $0.95 \times \min(U_{\text{STJ}}, U_{\text{PFJ}})$ where U_{STJ} and U_{PFJ} denote the 250-hPa $[\overline{u}]$ of the STJ and the PFJ, respectively. While somewhat arbitrary, the results described below show that the above criteria are consistent with one's visual impression.

Figure 4 shows the structural change of the jet as a function of $\mathcal{H}$ and C. Three types of jets—single, intermediate, and double jets—are indicated by circles with different shapes (see figure legend). The latitude and speed of the maximum $[\overline{u}]$ are also indicated in the figure. The single-jet and double-jet regimes are cross-hatched and the latitudinal profiles of 250-hPa $[\overline{u}]$, along the axes of A, B, C, and D, are illustrated. It is seen that, to a first order, the double-jet state, which is located at the bottom-right corner of the parameter space in Fig. 4, is favored in the small $\mathcal{H}$ and large C region. On the other hand, the single-jet state is favored for almost the entire parameter space with $\mathcal{H} > 0.67$ K day^{-1}. Although not shown in this study, the same $\mathcal{H}$–C parameter space was examined for $(T_o\Delta, T_o\Upsilon) = (60, 25)$ K and (80, 25) K. Both simulations yielded results qualitatively similar to that summarized in Fig. 4, indicating that the essential features of the results reported here are reasonably robust.

To further aid our analyses and presentation, we first identify four reference runs: intermediate jet (IJ), single jet (SJ), double jet (DJ), and additional single jet (SJ2). Each of these runs is indicated in Fig. 4 by black circles. Figure 5 shows the vertical structure of $[\overline{u}]$ for these reference runs. The SJ and SJ2 runs show just a single jet, although the jet in each run is a mix of a STJ and a PFJ (Figs. 5a and 5b). In the IJ run (Fig. 5c), there is

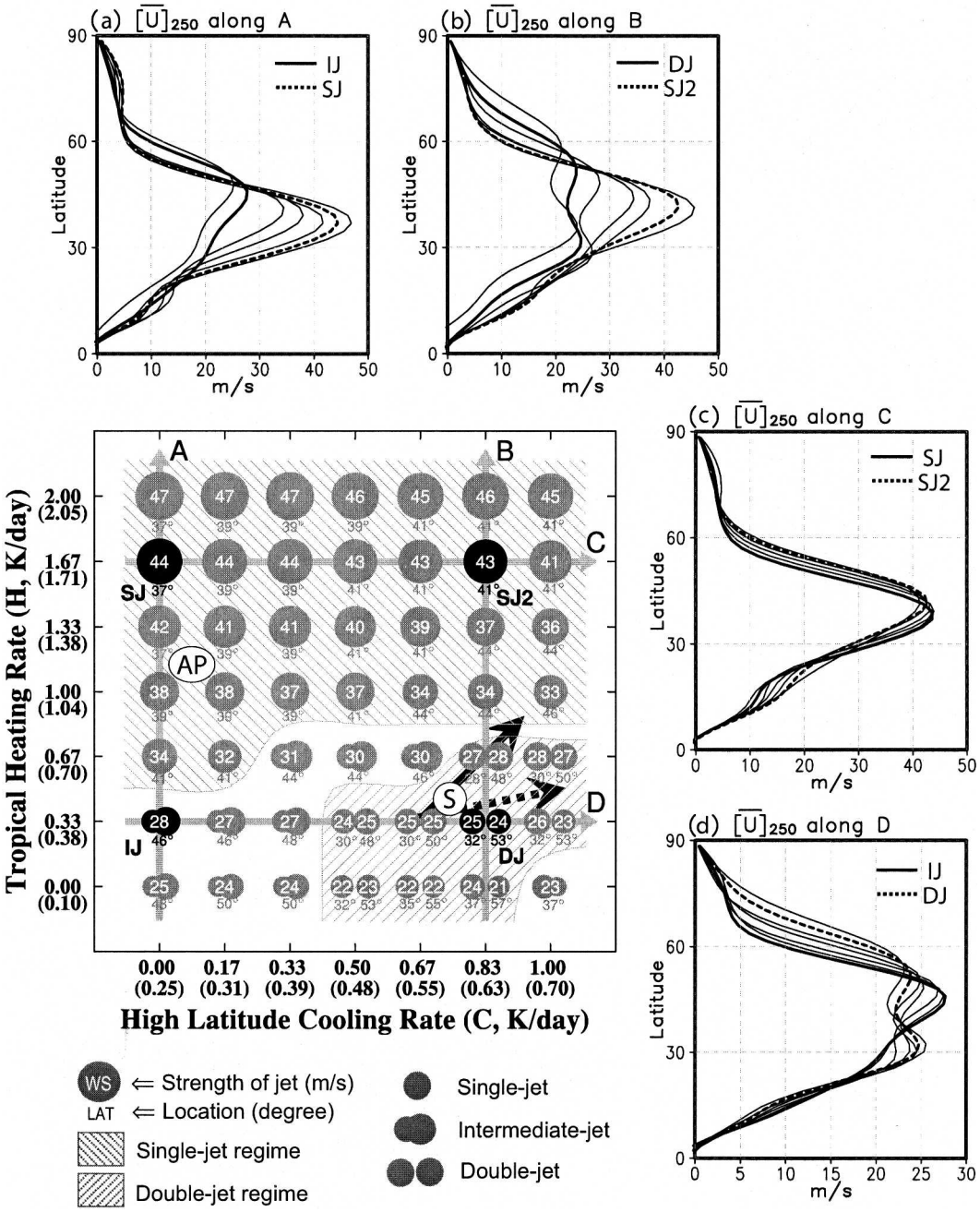

FIG. 4. Location and structure of the jet as a function of $\mathcal{H}$ and C. Along with the values of $\mathcal{H}$ and C, the vertical mean diabatic heating rate at the equator and cooling rate at the pole are given in parentheses on each axis. The figures surrounding the diagram show the latitudinal profile of 250-hPa $[\overline{u}]$ along the A, B, C, and D lines. For graphical purposes, only two reference states are denoted in each figure. See the text for details.

still no clear separation of the jets in the upper troposphere but there is a hint of two jets in the middle troposphere. Unlike the other jet profiles, $[\overline{u}]$ in the DJ run shows two distinct jets: a STJ at 32° and a PFJ at 52° (Fig. 5d).

As can be inferred from Figs. 4a and 4b, the intensification of the tropical thermal driving (i.e., the increase in $\mathcal{H}$) systematically strengthens and shifts the zonal-mean circulation equatorward. In contrast, the broadening of the extratropical baroclinic zone (i.e., the increase in C) gradually shifts the zonal-mean circulation poleward with minor changes in its strength (Figs. 4c

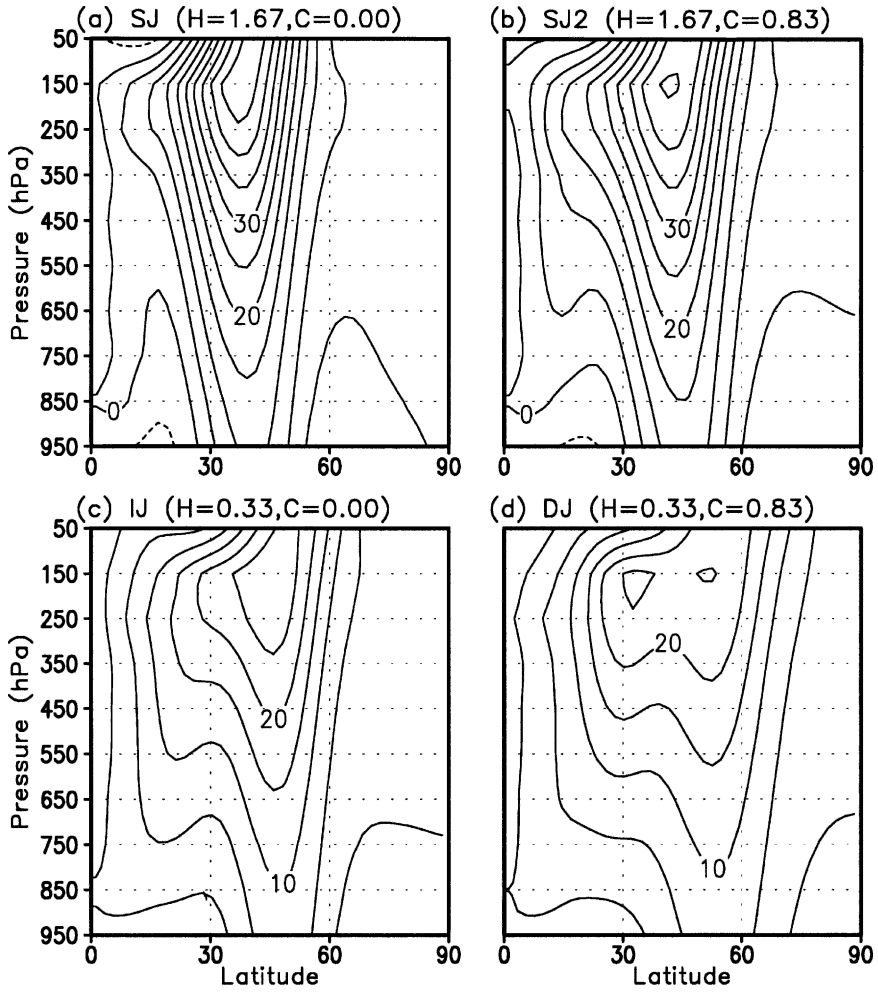

FIG. 5. The $[\overline{u}]$ in (a) SJ, (b) SJ2, (c) IJ, and (d) DJ runs. The contour interval is 5 m s^{-1}.

and 4d). These general responses of the jet to additional thermal forcings are further analyzed by comparing the SJ, IJ, and DJ runs (Figs. 5a, 5c, and 5d). In the quasigeostrophic framework, assuming linear dissipation, the zonal-mean zonal momentum equation can be expressed as

$$\frac{\partial [u]}{\partial t} = f[v] - \frac{1}{a\cos^2\varphi}\frac{\partial \cos^2\varphi [u^*v^*]}{\partial \varphi} - \frac{[u]}{\tau_d},$$

where f and τ_d are the Coriolis parameter and dissipation time scale, respectively. The asterisk denotes deviation from the zonal mean. The difference in $[\overline{u}]$ between any two statistically steady states, $\delta[\overline{u}]$, then takes the form

$$\delta[\overline{u}] = \tau_d\left\{f\delta[\overline{v}] - \delta\left(\frac{1}{a\cos^2\varphi}\frac{\partial \cos^2\varphi\overline{[u^*v^*]}}{\partial \varphi}\right)\right\}. \quad (2)$$

This relation[2] allows for an evaluation of the individual contributions by the mean-meridional circulation, $f\delta[\overline{v}]$,

[2] Since eddy momentum and heat fluxes do not act separately, the transformed Eulerian-mean (TEM) diagnostic (Andrews and McIntyre 1976) represents a true wave–mean flow interaction in the sense that zonal-mean flow change, for inviscid and adiabatic flows, can be expressed entirely in terms of the Eliassen–Palm (EP) flux (Eliassen and Palm 1961; Edmon et al. 1980), which combine both fluxes. However, we find that the difference in the EP flux divergence corresponds rather poorly with the $\delta[\overline{u}]$ field. This is due to a strong cancellation between the EP flux divergence and the TEM residual circulation (not shown). Instead, our results show a strong resemblance between $\delta[\overline{u}]$ and $-\delta\{a^{-1}\cos^{-2}\varphi\,\partial(\cos^2\varphi\overline{[u^*v^*]})/\partial\varphi\}$ [see (2)]; while $f\delta[\overline{v}]$ opposes $-\delta\{a^{-1}\cos^{-2}\varphi\,\partial(\cos^2\varphi\overline{[u^*v^*]})/\partial\varphi\}$, the magnitude of the former is smaller than that of the latter. These results are consistent with the findings of Pfeffer (1992) who noted that *tropospheric* zonal wind fluctuations are mainly caused by the horizontal component of the EP flux divergence that is associated with the eddy momentum flux. Since the goal of our diagnostic is to detect the role of the eddies on $\delta[\overline{u}]$ in the troposphere, we adopt the Eulerian-mean diagnostic of (2) rather than the TEM diagnostic.

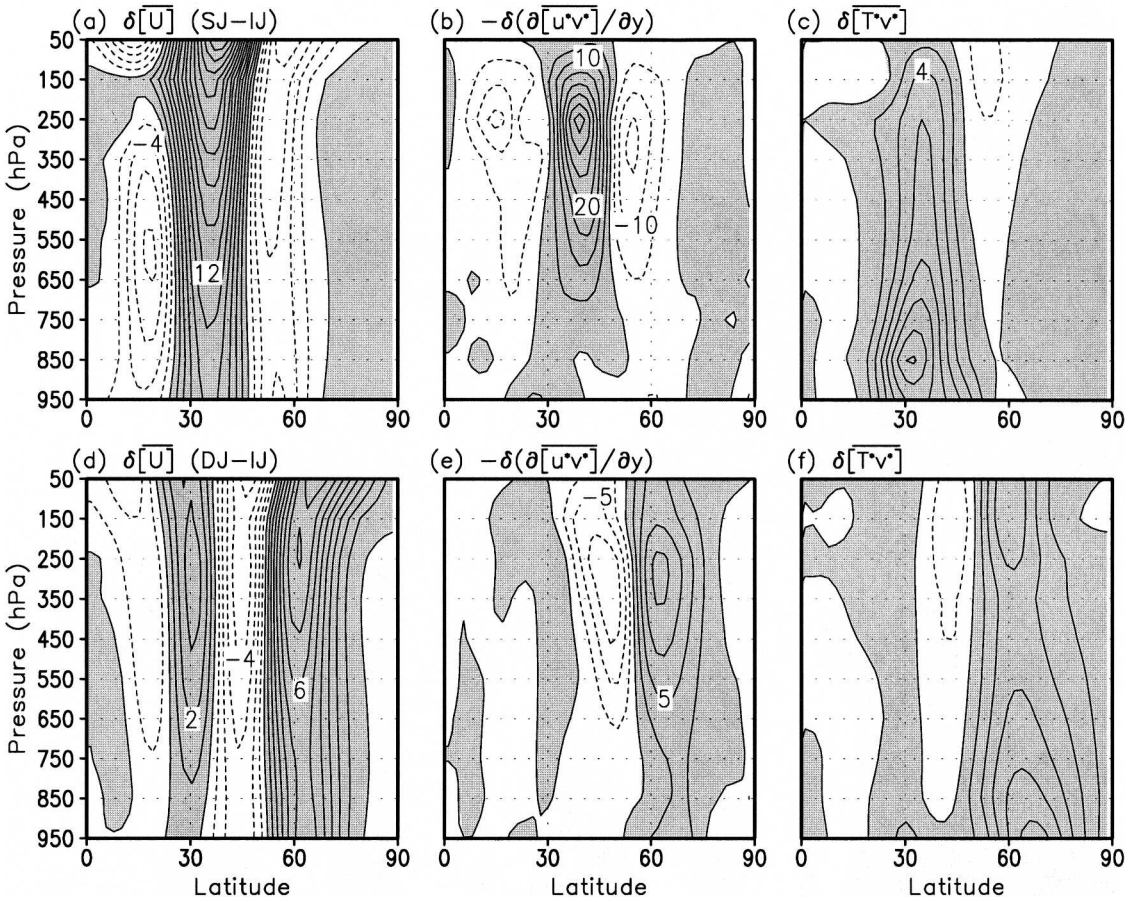

FIG. 6. Difference fields (top) between the SJ and IJ runs and (bottom) between the DJ and IJ runs: (left) $[\overline{u}]$, (center) eddy momentum flux convergence, and (right) meridional eddy heat flux. The contour intervals are (a) 2 m s^{-1}, (b) 5 $\times$ 10^{-6} m s^{-2}, (c) 2 K m s^{-1}, (d) 1 m s^{-1}, (e) 2.5 $\times$ 10^{-6} m s^{-2}, and (f) 1 K m s^{-1}. Positive values are shaded in all figures. In the figure titles of (b) and (e), the cos factors are ignored.

and the eddy flux, $\delta\{a^{-1}\cos^{-2}\varphi\,\partial(\cos^2\varphi\overline{[u^*v^*]})/\partial\varphi\}$. The $\delta[\overline{u}]$ between the SJ and IJ runs is displayed in Fig. 6a. It shows a quasi-barotropic structure poleward of 30°, suggesting that the circulation change in the extratropics is dominated by changes in the eddy fluxes. Indeed, poleward of 30°, the difference in eddy momentum flux convergence (Fig. 6b) closely resembles $\delta[\overline{u}]$ (Fig. 6a). This arises from the fact that the more intense tropical heating in the SJ run generates a stronger Hadley circulation, which then tightens meridional temperature gradient at its poleward boundary (although not shown, this is apparent in runs with the axisymmetric version of the model). Consistent with this increase in subtropical baroclinicity, we observe that the meridional eddy heat flux for the SJ run is stronger throughout the troposphere, particularly at the poleward vicinity of the Hadley circulation (Fig. 6c). This equatorward shift in the eddy fluxes brings the PFJ close to the STJ, blending the two jets together.

As described earlier, the poleward expansion of the baroclinic zone transforms the IJ into a DJ. This transition is consistent with changes in the eddy activity, which also shifts poleward (Fig. 6f). At the same time, a reduction in wave drag in the Tropics and subtropics is consistent with the stronger STJ (Fig. 6d). Once again, $\delta[\overline{u}]$ in the extratropics is highly congruent with the changes in the eddy momentum flux convergence (Fig. 6e). Note that this type of overall response to an increase in C holds only for $\mathcal{H} < 0.67$ K day^{-1}. Otherwise, as stated earlier, a single-jet state is maintained regardless of the value of C, suggesting that with sufficiently strong tropical heating the circulation is rather insensitive to extratropical baroclinicity.

Figure 4 also shows that the boundary between the single- and the double-jet regimes is often sharp. For instance, as shown in Fig. 4b, a steep transition occurs when $\mathcal{H}$ crosses from 0.67 to 1.00 K day^{-1}. This threshold behavior is qualitatively similar to LK03, and will be examined more closely in section 6.

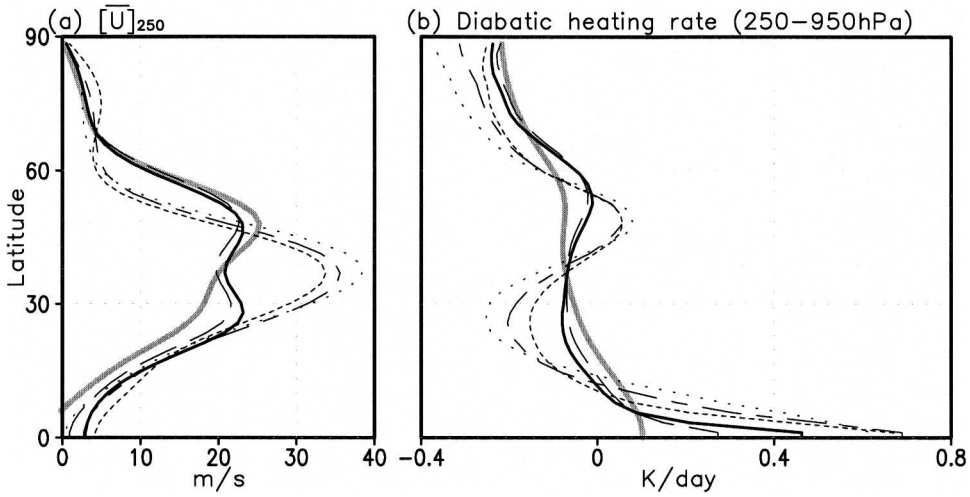

FIG. 7. (a) Latitudinal profiles of 250-hPa $[\overline{u}]$ and (b) vertical mean diabatic heating rates for 75% (long dashed), 80% (thick solid), 85% (short dashed), 90% (long–short dashed), and 100% (dotted lines) moist runs, and for the dry base run (thick gray lines).

4. Effect of latent heating

This section examines a few selected cases from the moist model and compares the results to those from the $\mathcal{H}$–C parameter space. Such a comparison serves two purposes: first, it helps us to understand how the latent heating alters the large-scale circulation; second this understanding in turn can improve our ability to interpret and possibly to predict general circulation responses to global warming scenarios.

For the comparison with the results from the $\mathcal{H}$–C parameter study of the previous section, which was performed with the dry model, the basic configuration of the moist model is identical to that of the base run of the dry model. That is, as stated in section 2d, for all moist runs to be examined below, values of both $\mathcal{H}$ and C are set equal to zero. Instead, the additional (in addition to the relaxation to the radiative equilibrium state) thermal driving now takes the form of latent heating, generated spontaneously by the moist model.

In our model, the overall intensity of the latent heating is controlled by the total amount of moisture prescribed for the model atmosphere. As a reference, the amount of moisture in the model atmosphere is specified as a percentage of the NCEP–NCAR annual-mean specific humidity. When the model is prescribed with this amount of moisture, we refer to this calculation as the 100% moist run. To this end, we need to point out some of the key limitations of this model that are crucial for proper interpretation of the model results. First, because the radiative equilibrium state of this moist model already includes some of the latent heating effect (cf. radiative–convective equilibrium), while the specific humidity is based on the observed values, it is likely that the effect of latent heating is exaggerated in the 100% run. Second, we emphasize that the physical parameterizations used in this study are simple enough to be readily understood, but that it comes with cost. For example, the form of the parameterized cloud-induced radiative cooling, described in section b of the appendix, is very crude and arbitrary. If the value of the parameter R in (A2) is chosen to be less than 100 K day^{-1}, which is used throughout this study, the details of the results to be summarized in Fig. 7 change. The transition between the double- and single-jet states no longer takes place across the 80%–85% runs, but instead occurs at higher values of the moisture content. Therefore, the 100% run should not necessarily be expected to generate the most realistic circulation. We also note that the goal of this study is not to simulate the atmosphere as well as possible, but to investigate the circulation response to the latitudinal distribution of the heating.

Figures 7a and 7b show the 250-hPa $[\overline{u}]$ and vertical mean diabatic heating rates (= latent heating + Newtonian cooling), respectively, from five separate runs with differing moisture contents. Here, the vertical mean quantity is calculated by using data from 250 to 950 hPa. It can be seen that, as moisture is added to the dry base run, the intermediate-jet state (see Fig. 3a) first evolves to a double-jet state (see the 75% and 80% runs in Fig. 7a). As the moisture content is further increased from 80% to 85%, the two jets suddenly collapse into a single jet (see Fig. 7a), resembling the threshold behavior observed in the dry runs (Fig. 4b).

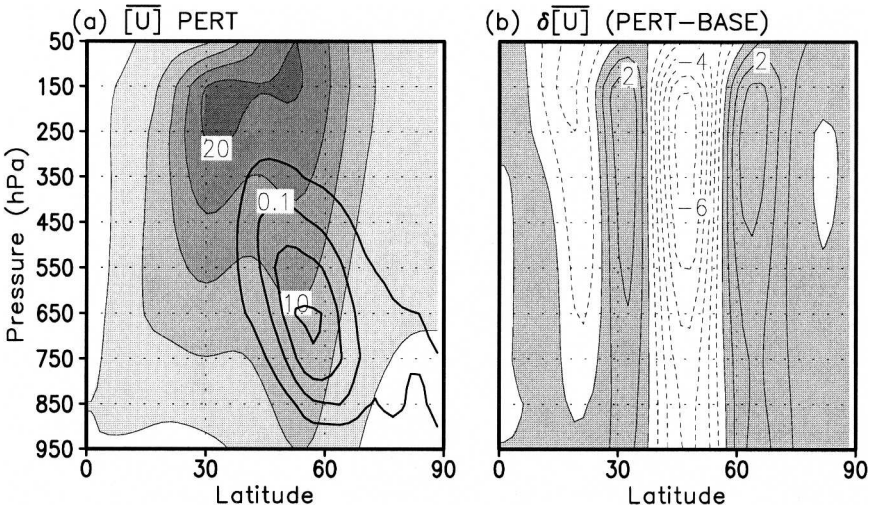

FIG. 8. (a) Plot of $[\overline{u}]$ in the PERT run. Superimposed is the added value of midlatitude heating, which is derived from the 80% moist run. The shading and contour intervals are 5 m s^{-1} and 0.05 K day^{-1}, respectively. (b) Difference in $[\overline{u}]$ between the PERT and the base runs. The contour interval is 1 m s^{-1}. Positive values are shaded.

Moreover, the threshold values in the tropical diabatic heating rate are also consistent with the dry model results. For a moisture content above 85%, for which the flow is characterized by a single jet, the tropical diabatic heating rate is greater than ≈0.66 K day^{-1}. In the dry runs, the value of $\mathcal{H}$ for the same threshold is in between 0.67 and 1.00 K day^{-1}.

The above circulation response to the moisture content is rather complex in that a relatively small amount of moisture prefers a double-jet state, while any further increase in moisture, beyond a certain critical value, degenerates the jets into a single-jet state. In what follows, with the aid of the $\mathcal{H}$–C parameter study, we attempt to provide a plausible explanation for that response. From the diabatic heating rates shown in Fig. 7b, it can be inferred that the latent heating in midlatitudes tends to increase the extratropical baroclinicity poleward of ~55°, while that in the Tropics enhances tropical thermal driving. Taken together, the relationship between the $[\overline{u}]$ in moist model runs and the relative role of the tropical and midlatitude diabatic heating is reasonably consistent with the circulation characteristics in the $\mathcal{H}$–C parameter space; when the tropical latent heating is moderate (the 75% and 80% moist runs), the broadening of the extratropical baroclinic zone, due to midlatitude latent heating, drives the circulation toward the double-jet state. In that sense, the midlatitude latent heating plays a role dynamically equivalent to that of the extra high-latitude cooling. With a further increase in the moisture content to 85%, however, the intensified tropical thermal driving resulting from the tropical latent heating overwhelms the effect of the midlatitude latent heating, turning the double jet into a single-jet state.

We next test the above postulation that the midlatitude moist heating and the high-latitude cooling (C) are dynamically equivalent. To do so, an additional dry model run is performed. In this run (hereafter PERT), a new T_e profile is constructed by adding the time-mean zonal-mean extratropical latent heating of the 80% moist run to the base T_e profile. The 80% moist run is chosen because its $[\overline{u}]$ is qualitatively similar to the observed equinoctial SH jet. Although not shown, a similar dry model run with both tropical and extratropical latent heating reproduces the 80% moist run with reasonable accuracy. A comparison of $[\overline{u}]$ in the PERT run (Fig. 8a) with that in the base run (Fig. 3) indicates that the role of the extratropical moist heating is to move the PFJ poleward, separating it from the STJ. The difference field between the PERT and the base runs (Fig. 8b) further shows that the response of $[\overline{u}]$ to the midlatitude moist heating is quasi barotropic, indicating that the response is realized through midlatitude eddy fluxes. This difference field also broadly resembles Fig. 6d, strongly suggesting that the midlatitude latent heating plays a role similar to the dry model's high-latitude cooling.

Given the above evidence that the model response to the moisture content variation can be interpreted in the context of the $\mathcal{H}$–C parameter space, it is useful to identify where in the $\mathcal{H}$–C parameter space each of the moist runs lie. Because C in the dry run and the midlatitude latent heating in the moist run cannot be quantitatively

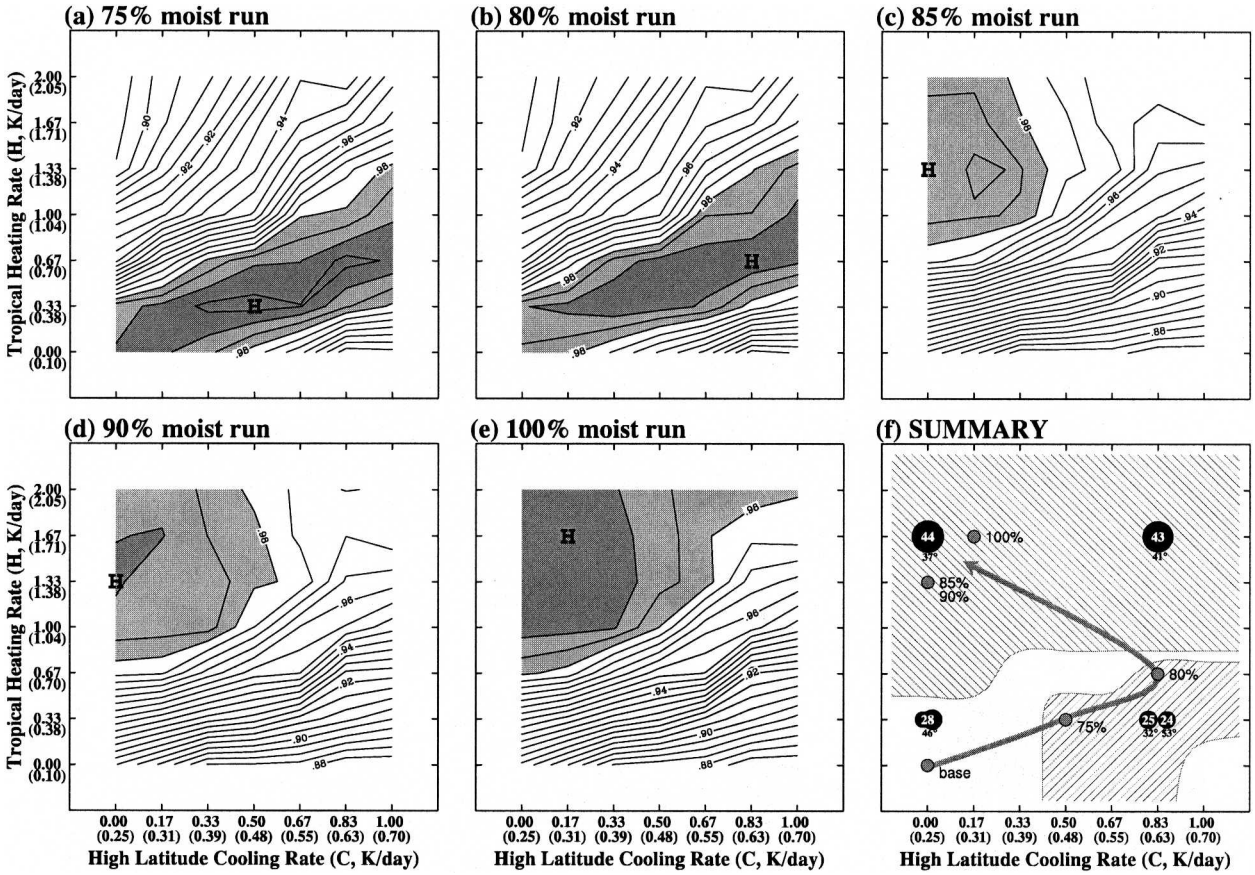

FIG. 9. The pattern correlation between $[\overline{u}]$ of each of the dry runs in Fig. 4 and the (a) 75%, (b) 80%, (c) 85%, (d) 90%, and (e) 100% moist runs. Correlation coefficients greater than 0.98 are shaded. The gray circles in (f) and H in other figures indicate the locations where the maximum pattern correlation coefficients take place. For ease of comparison with Fig. 4, (f) also shows the single- and double-jet regimes (hatched area), and the IJ, DJ, SJ, and SJ2 cases.

compared, we instead choose to make the identification based on similarity in jet structure. The similarity is objectively measured by a pattern correlation of $[\overline{u}]$ between each of the dry and the moist runs. This calculation results in five separate pattern-correlation maps (Figs. 9a–e) covering the same domain as in Fig. 4. Starting from the base run, which is at the bottom left corner of the domain, as the moisture content is increased to 75%, and then to 80%, the location of highest pattern correlation moves toward the double-jet regime (see Figs. 9a and 9b; for a summary see Fig. 9f). However, for moisture contents higher than 85%, the highest pattern correlation takes place in the upper-left corner of the domain (Figs. 9c–e). Thus, as summarized in Fig. 9f, the path taken by the moist run is monotonic in $\mathcal{H}$, but not in C. This result indicates that while $\mathcal{H}$ mimics the tropical latent heating throughout the entire $\mathcal{H}$–C domain, the similarity between the dynamical impact of C and that of the midlatitude heating is apparent only when the $\mathcal{H}$ is rather weak.

5. Comparison between the initial value problems and the statistically steady states

The results from the analysis of the statistically steady states in sections 4 and 5 are broadly consistent with both the linear and the initial-value calculations of LK03. They showed that as the tropical heating rate is gradually varied, the jet structure abruptly changes across a certain threshold value. This section investigates to what extent linear theory can predict the statistically steady states and what process explains their differences.

As in LK03, an axisymmetric circulation is calculated by integrating an axisymmetric version of the PE model forward in time. Once a steady-state axisymmetric circulation is obtained, the divergence field is set to zero and the vorticity field is nonlinearly balanced to the temperature and surface pressure fields (Branscome et al. 1989). The meridional wind is set to zero in this process, but the modification of the zonal wind is small.

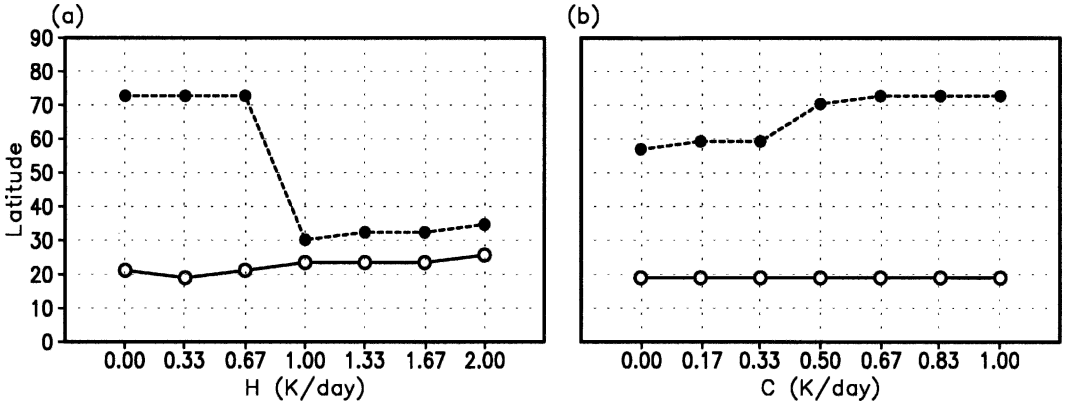

FIG. 10. Latitudes of the axially symmetric steady-state STJs (open) and corresponding PFJs (closed circles) obtained from the linear calculations: (a) is for line **B** and (b) for line **D** in Fig. 4.

With this background state, the normal mode analysis is performed with zonal wavenumber 5, which is typically the dominant zonal wave for the statistically steady states. In this linear calculation, the location of the PFJ is defined by the latitude of maximum eddy momentum flux convergence of the most unstable normal mode.

The linear theory predicts that, following line B of Fig. 4, the transition from a double jet to a single-jet state takes place as the $\mathcal{H}$ value crosses from 0.67 to 1.00 K day^{-1} (Fig. 10a). This is consitent with the result of statistically steady states (Fig. 4b). For line D, the linear result shown in Fig. 10b predicts a double-jet state for all values of $\mathcal{C}$. On one hand, this is at odds with the statistically steady-state result where the transition from an intermediate jet to a double jet takes place as the $\mathcal{C}$ value crosses from 0.33 to 0.50 K day^{-1}. On the other hand, the linear and the statistically steady-state results are consistent in the sense that the two jets predicted by the linear calculation are closer together (farther apart) for $\mathcal{C} \leq 0.33$ K day^{-1} (≥ 0.5 K day^{-1}) where intermediate-jet (double jet) states prevail in the statistically steady state (see Fig. 4).

As such, while the linear theory and initial-value calculations are able to predict the qualitative behavior of the equilibrium jet, it is also clear that the transition is not as dramatic as that in the linear theory. This discrepancy is analyzed with spectral analysis (Hayashi 1971; Randel and Held 1991). Figures 11a–c show the phase speed spectrum of the 250-hPa eddy momentum flux convergence for cases along line D of Fig. 4. For a finer spectral resolution, output from the R30 simulations are analyzed here. Although not shown, there is no qualitative difference between the resulting spectrum and that from the corresponding R15/30 run. The location and magnitude of the jets from these runs, superimposed in Figs. 11a–c, are again almost identical to those obtained from the R15/30 run (see Fig. 4d).

One notable feature in the top panels of Fig. 11 is that, as the width of the baroclinic zone increases (i.e., as the value of $\mathcal{C}$ increases), a scale separation in the zonal phase speed c starts to take place; there is an apparent spectral gap between fast waves ($c > 10$ m s^{-1}) and slow waves ($c < 10$ m s^{-1}). As this scale separation occurs, the fast wave contribution to $[\overline{u}]$ becomes different from the slow wave contribution. This behavior can be succinctly seen in Figs. 11e and 11f, which illustrate the contribution of the slow (5.0 m s^{-1} $\leq c \leq$ 9.5 m s^{-1}) and that of the fast (11.0 m s^{-1} $\leq c \leq$ 15.5 m s^{-1}) waves to the total eddy momentum flux convergence (Fig. 11d). As the baroclinic zone broadens, while the contribution from the slow waves remains almost identical, that from the fast-moving waves exhibits a systematic poleward shift. Comparing the three curves in Fig. 11f with the corresponding $[\overline{u}]$ shown in Figs. 11a–c, it is clear that the location of the PFJ is determined by the fast waves. In contrast, the slowly propagating waves, which result from the low-frequency variability hence are absent both in the linear and the initial-value calculations (LK03), act to blend the PFJ and the STJ, by depositing eastward momentum between the two jets, and westward momentum in the subtropics and Tropics. This result is consistent with the fact, as stated above, that for $\mathcal{C} < 0.5$ K day^{-1} along line D, the jets are still well separated in the linear calculation (Fig. 10b), but the nonlinear statistically steady state show only an intermediate jet. Essentially the same result is found for the cases along line B.

6. Summary

This study examined the dynamic relation between subtropical and polar-front jets. The results of this

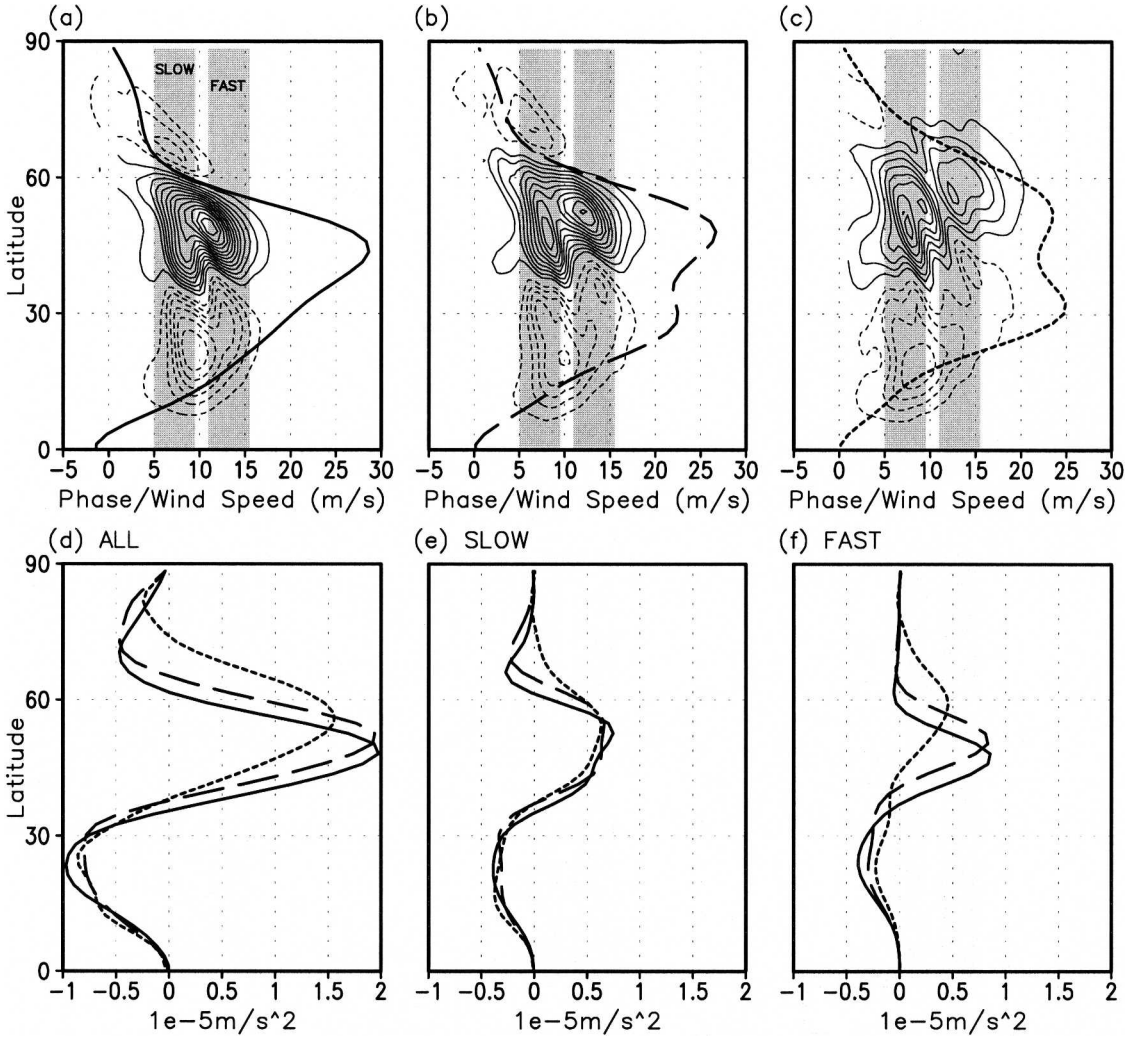

FIG. 11. The phase speed spectra of 250-hPa eddy momentum flux convergence for selected cases along the line **D** in Fig. 4: (a) $C = 0.00$ K day^{-1} (IJ run), (b) $C = 0.33$ K day^{-1}, and (c) $C = 0.83$ K day^{-1} (DJ run). The contour interval is 4×10^{-8} m s^{-2}. Superimposed thick lines in (a)–(c) are the associated 250-hPa $[\overline{u}]$. The bottom panels show the corresponding eddy momentum flux convergence integrated over (d) all phase, (e) the slow phase, and (f) the fast phase speeds. The range of slow and fast waves is depicted in (a)–(c). In (d)–(f), the solid lines correspond to (a), the long-dashed lines to (b), and the short-dashed lines to (c).

study find that statistically steady-state calculations yield results that are broadly consistent with the dynamic relationship obtained from both the linear and the initial-value calculations by LK03. It is found that a double-jet state is favored when tropical heating, hence the subtropical jet, is weak and high-latitude cooling is strong. In general, the opposite behavior is the case for a single-jet state. The results from this study also indicate that a broad extratropical baroclinic zone is required for the existence of a double-jet state. This condition was not required in the initial-value calculations performed by LK03, but appears to be consistent with the observed seasonal evolution of the zonal-mean temperature field and the attendant jet structure in the SH.

Compared with the initial-value calculations (not shown in this study; see LK03), the double-jet state forms less readily in the statistically steady state. The cross-spectral analysis suggests that this difference can be attributed to the slow waves (Lee 1997; Kim and Lee 2004), which are absent in the initial-value calculations. The momentum flux from the fast, or high-frequency, waves would drive a separate PFJ, but that from the slow, or low-frequency, waves blends this would-be PFJ and the STJ by depositing eastward (westward) momentum between the two jets (in the subtropics and

Tropics).[3] Therefore, in order for the double-jet state to be maintained against the action of the low-frequency waves, the high-frequency driving must take place farther poleward. For the same reason, in the statistically steady states, the transition from double-jet to single-jet states is not as dramatic as its counterpart in the initial value problem (LK03) or in the linear normal mode solutions (LK03; see also Fig. 10). Nonetheless, at least in the idealized PE model used in this study, the transition points in the $\mathcal{H}$–C space are reasonably well predicted by the linear normal mode solutions.

Although the midlatitude heating and high-latitude cooling are different processes, a set of moist model runs suggests that the two effects are, to first order, dynamically equivalent in the sense that they both broaden extratropical baroclinic zone. Starting from dry base run, when the moist process is allowed in the model with moderate amount of moisture, the intermediate jet is first replaced by a double jet. Based on the insight gained from the $\mathcal{H}$–C parameter study, we interpret this result as being a consequence of the increased high-latitude baroclinicity arising from the midlatitude latent heating. As the moisture content is gradually increased, the double-jet state is then collapsed into a single-jet state. Again, this is consistent with the result of the $\mathcal{H}$–C parameter study since, when tropical heating is greater than a certain threshold value, which indeed takes place as the moisture content is increased, the circulation always falls onto a single-jet state, regardless of the C value.

7. Implications for climate change

While the dynamical framework of zonally homogeneous statistics cannot be strictly applied to the atmosphere, additional calculations, which are not shown in the main text but will be described below, suggest that such a dynamical framework may be applicable for the SH and also for the NH East Asian–Pacific sector. When the dry model was driven toward an empirical zonal-mean equilibrium temperature field for the SH winter, we found that the observed zonal-mean winter circulation was faithfully reproduced (see also Kim and Lee 2004). It was also found that the effect of surface sensible heat flux in the model, which is ignored, was rather minor (see also Becker and Schmitz 2001; Kim and Lee 2001). Following the method of Lunkeit et al. (1998), we also reproduced a circulation qualitatively similar to the observed NH flow averaged from 90°E to 180°, by relaxing the model flow toward the observed temperature field averaged over the same region. However, the same calculation applied for the Atlantic region was unable to reproduce the observed circulation. Thus, the rest of the discussion is restricted to circulations for the SH and for the NH Asian–Pacific sector. In addition, since the model's maximum heating is at the equator, the emphasis will be placed on equinoctial conditions.

Keeping the above limitation in mind, we now attempt to interpret and predict atmospheric responses to changes in the thermal driving. In Fig. 4, we identify two regions, denoted as AP and S, relevant for the NH East Asian–Pacific jet and the SH equinoctial zonal-mean jet, respectively. These approximate locations in the parameter space are determined subjectively based on morphological similarities in the latitude and intensity of the jets. According to this subjective analysis, the jet over the NH East Asian–Pacific sector (AP) is situated well into the middle of the single-jet regime, while the SH jet (S), although located in the double-jet regime, is adjacent to the border with the other two regimes, that is, the intermediate- and single-jet regimes. This implies that in response to changes in the thermal field, the SH circulation will be more sensitive than the circulation over the NH East Asian–Pacific sector. This is indeed consistent with the interannual variability of westerly jet. While the NH East Asian–Pacific jet does not undergo any substantial structural change, the SH jet does (e.g., Ambaum et al. 2001).

Kushner et al. (2001) show with an atmosphere–ocean coupled model that, in response to a doubling of the atmospheric CO_2 content, the SH circulation evolves into a more distinct double-jet state for all seasons. The CO_2-induced global warming drives an ENSO-like tropical response (Kushner et al. 2001; IPCC 2002). In the SH, the amount of warming decreases toward a local minimum between 60° and 70°S and then increases farther poleward (Kushner et al. 2001; IPCC 2002). This local minimum results from an intensified upwelling of cold water in the Southern Ocean (e.g., Manabe and Stouffer 1988). While the baroclinicity of the subpolar regions decreases due to warming at Antarctica, it is found that the jet structure is insensitive to the baroclinicity in this region.[4] There-

[3] The statistics of the slow and fast transient waves, however, may be sensitive to realistic stationary wave forcing, which is absent in our study.

[4] To test the impact of subpolar baroclinicity on jet structure, an additional model run is performed. The T_e profile for this simulation is same as that for the DJ run (long-dashed lines in Fig. 2a) except at latitudes higher than 70°. In this region, T_e is modified to have a positive meridional gradient. The westerly jet in this run is found to be qualitatively similar to that in DJ run, indicating that subpolar baroclinicity plays a minimal role.

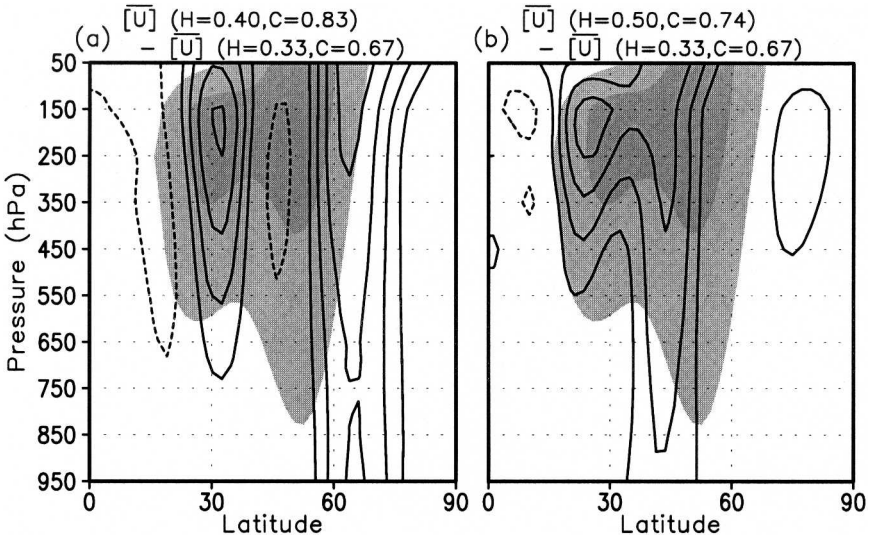

FIG. 12. Changes in $[\overline{u}]$ when $(\Delta\mathcal{H}, \Delta C)$ are increased by (a) (0.07, 0.17) and (b) (0.17, 0.07) K day^{-1}. Contour intervals are 0.5 m s^{-1} and zero lines are omitted. Superimposed in both figures are $[\overline{u}]$ when $(\mathcal{H}, C) = (0.33, 0.67)$ K day^{-1}. Shading interval is 10 m s^{-1} starting from 10 m s^{-1}.

fore, in the context of our study, the temperature response in Kushner et al. (2001), strong warming in the Tropics and a local minimum in the warming at high latitudes, can be interpreted as a strengthened tropical thermal driving (increase in $\mathcal{H}$) and an enhanced extratropical surface baroclinicity (increase in C). According to Fig. 4 then, if the impact of the CO_2-induced tropical heating is less significant than the impact of the CO_2-induced extratropical baroclinicity, that is, if $\Delta\mathcal{H} < \Delta C$, the circulation is more likely to remain in a double-jet state (Fig. 12a, also see the thick dotted arrow in Fig. 4). On the other hand, if $\Delta\mathcal{H} > \Delta C$ (Fig. 12b, also see the thick solid arrow in Fig. 4), the circulation is likely to evolve toward a single-jet state. The circulation change in Fig. 12a is very similar to the coupled GCM response (Kushner et al. 2001, see their Fig. 4), suggesting that the GCM response can be interpreted as a consequence of the impact of the increase in the extratropical baroclinicity being greater than that of the increase in the tropical heating.

The results from the moist run facilitate further speculation. As the atmosphere warms, the hydrological cycle intensifies (e.g., Ziegler et al. 2003), amplifying the overall latent heating. Considering this moisture effect alone, a run with a higher moisture content, relative to a control run with a lower moisture content, may be viewed as a global warming scenario run. This raises the possibility that with a further greenhouse gas warming, the effect of the elevated tropical heating may eventually dominate the combined effect of the increased midlatitude latent heating and high-latitud cooling (provided that the ocean upwelling in the Southern Ocean maintains the low sea surface temperature), shifting the circulation into the single-jet regime. For example, starting from a control circulation that resembles the dry base run, one may envision that an incremental global warming guides the circulation along the path taken by the moist runs (see the curve in Fig. 8f). The point is that knowledge of the parametric behavior of the climate states can be highly useful for understanding and predicting the circulation response to the temperature changes.

Acknowledgments. Discussion with Dr. Steven Feldstein in the early stage of this work is gratefully appreciated. We also thank Dr. Erich Becker for useful comments that improved this manuscript. This research was supported by the National Science Foundation through Grant ATM-0324908.

APPENDIX

Moist Processes

The latent heating is represented by a moist-convective adjustment and large-scale condensation (Manabe et al. 1965). The model does not include a comprehensive radiation scheme although it is still driven by the radiative relaxation. This set of idealizations, while compatible with the dry model, generates an unrealistic feature (see below). In addition, the model produces negative humidity as a by-product of

the spectral truncation. These shortcomings are dealt with by using the following treatments.

a. Specific humidity correction

The spectral truncation itself generates unphysical negative moisture. To remove this artifact, the negative specific humidity at each gird point is set to zero by borrowing moisture from the neighboring grids. This is realized by transferring an amount of moisture Δq (see definition below) from positive to negative specific humidity grids. If the specific humidity of the neighboring grid is less than Δq, it yields all available moisture to the negative specific humidity grids. Then, the entire adjustment process is repeated from pole to equator until negative specific humidity is entirely removed. The moisture borrowing function is

$$\Delta q(\lambda, \varphi) = -\sum_{\varphi} \min\{0, q(\lambda, \varphi)\}\, W(\varphi|\lambda), \qquad \text{(A1)}$$

where

$$W(\varphi|\lambda) = \begin{cases} \dfrac{|\sin\varphi|}{\sum\limits_{\varphi} |\sin\varphi|}, & \text{if} \quad q(\lambda, \varphi) > 0 \\ 0, & \text{otherwise.} \end{cases}$$

This method is similar to that of Gordon and Stern (1982) except for the form of the weighting function. If the moisture is exchanged only between several neighboring grid points, as in Gordon and Stern, the procedure generates a broad zone of zero specific humidity around the pole. This shortcoming is exacerbated in the axisymmetric version of the model. The form of the weighting function in (A1) removes this unrealistic feature by sharing moisture over a wider latitudinal range.

b. Diabatic heating correction

The moist-convective adjustment and large-scale condensation are applied only below 250 hPa. These adjustments are initiated when the relative humidity at a given grid point is greater than 100%. With this simple configuration, a test run was performed with an axisymmetric version of the model. This test showed unrealistically rapid, small-scale fluctuations in all model variables. It was determined that grid-scale heating is the culprit of these unrealistic features. The grid-scale heating, in turn, is a result of a positive feedback between convective heating and an associated overturning circulation, and this positive feedback continues until all available moisture near the heating maximum is exhausted.

In the real atmosphere, such a positive feedback loop is limited by an interactive radiative cooling associated with clouds that is, to first order, proportional to the intensity of the convection. However, the radiative cooling in our model is controlled by a somewhat arbitrary parameter τ_R. Because a τ_R value of 30 days is much larger than an instantaneous moist-convective adjustment time scale, and more importantly because τ_R is held constant, the relaxation scheme is incapable of mimicking the radiative cooling associated with the convection. This model deficiency is treated by including a correction factor R, which controls the effective heating rate Q_{eff} realized by the convective adjustment process Q_c,

$$Q_{\text{eff}} = Q_c \exp\left[-\left(\frac{Q_c}{R}\right)^{1/2}\right], \qquad \text{(A2)}$$

where the value of R is set equal to 100 K day^{-1}. This particular form of the correction factor, while based on the above physical process, is chosen arbitrarily. With this correction factor, the moist model yields a more realistic diabatic heating field.

Some quantitative results in section 5 are sensitive to the choice of R. For example, for the 80% moist run, if Q_{eff} is set equal to Q_c, the double-jet state is replaced by a single-jet state (not shown). However, the double-jet states still exist for the 75% moist run. Also, the transition between the two states is still abrupt, indicating that the correction factor does not change the qualitative results.

c. Evaporation and subgrid-scale mixing

The evaporation profile, E, is explicitly calculated by assuming that total precipitation at a given time step, P, evaporates instantaneously,

$$E(\lambda, \varphi) = \sum_{\lambda,\varphi} P(\lambda, \varphi) \times \frac{e(\lambda, \varphi)}{\sum\limits_{\lambda,\varphi} e(\lambda, \varphi)}, \qquad \text{(A3)}$$

where the evaporation function, following Gutowski et al. (1992), takes the form of

$$e(\lambda, \varphi) = \rho_s(\lambda, \varphi) V_s(\lambda, \varphi)[q_s^*(\lambda, \varphi) - q_s(\lambda, \varphi)].$$

Here, ρ_s is the density, V_s the wind speed, q_s the specific humidity, and q_s^* the saturated specific humidity for the equilibrium temperature, with the subscript s denoting the model's bottom layer. The relation (A3) states that at all times the globally integrated evaporation is set equal to the globally integrated precipitation. Accordingly, the amount of moisture, integrated over the entire model atmosphere, is conserved.

The initial specific humidity field takes the form

$$q(\lambda, \varphi, \sigma) = \Lambda q_e^*(\lambda, \varphi, \sigma) \frac{\sigma}{\sigma_s},$$

where Λ is a constant coefficient that controls the moisture content of the atmosphere, and q_e^* is the saturated specific humidity for the equilibrium temperature. Lastly, mixing by subgrid-scale processes is represented by second-order horizontal diffusion where the value for the diffusion coefficient is set equal to $2.5 \times 10^5\ \mathrm{m^2\ s^{-1}}$.

REFERENCES

Ambaum, M. H. P., B. J. Hoskins, and D. B. Stephenson, 2001: Arctic oscillation or North Atlantic oscillation? *J. Climate,* **14,** 3495–3507.

Andrews, D. G., and M. E. McIntyre, 1976: Planetary waves in horizontal and vertical shear: The generalized Eliassen–Palm relation and mean zonal acceleration. *J. Atmos. Sci.,* **33,** 2031–2048.

Becker, E., and G. Schmitz, 2001: Interaction between extratropical stationary waves and the zonal mean circulation. *J. Atmos. Sci.,* **58,** 462–480.

Branscome, L. E., W. J. Gutowski Jr., and D. A. Stewart, 1989: Effect of surface fluxes on the nonlinear development of baroclinic waves. *J. Atmos. Sci.,* **46,** 460–475.

Edmon, H. J., B. J. Hoskins, and M. E. McIntyre, 1980: Eliassen–Palm cross sections for the troposphere. *J. Atmos. Sci.,* **37,** 2600–2616.

Eliassen, A., and E. Palm, 1961: On the transfer of energy in stationary mountain waves. *Geofys. Publ.,* **22,** 1–23.

Gordon, C. T., and W. F. Stern, 1982: A description of the GFDL global spectral model. *Mon. Wea. Rev.,* **110,** 625–644.

Gutowski, W. J., L. E. Branscome, and D. A. Stewart, 1992: Life cycle of moist baroclinic eddies. *J. Atmos. Sci.,* **49,** 306–319.

Hayashi, Y., 1971: A generalized method of resolving disturbances into progressive and retrogressive waves by space Fourier and time cross-spectral analysis. *J. Meteor. Soc. Japan,* **49,** 125–128.

Held, I. M., and A. Y. Hou, 1980: Nonlinear axially symmetric circulations in a nearly inviscid atmosphere. *J. Atmos. Sci.,* **37,** 515–533.

Hoskins, B. J., 1983: Modeling of the transient eddies and their feedback on the mean flow. *Large-Scale Dynamical Process in the Atmosphere,* B. J. Hoskins and R. P. Pearce, Eds., Academic Press, 169–199.

IPCC, 2002: *Climate Change 2001 Synthesis Report.* Cambridge University Press, 397 pp.

James, I. N., 1994: *Introduction to Circulating Atmospheres.* Cambridge University Press, 422 pp.

——, and L. J. Gray, 1986: Concerning the effect of surface drag on the circulation of a baroclinic planetary atmosphere. *Quart. J. Roy. Meteor. Soc.,* **112,** 1231–1250.

Kim, H.-K., and S. Lee, 2001: Hadley cell dynamics in a primitive equation model. Part I: Axisymmetric flow. *J. Atmos. Sci.,* **58,** 2845–2858.

——, and ——, 2004: The wave–zonal mean flow interaction in the Southern Hemisphere. *J. Atmos. Sci.,* **61,** 1055–1067.

Kushner, P. J., I. M. Held, and T. L. Delworth, 2001: Southern Hemisphere atmospheric circulation response to global warming. *J. Climate,* **14,** 2238–2249.

Lee, S., 1997: Maintenance of multiple jets in a baroclinic flow. *J. Atmos. Sci.,* **54,** 1726–1738.

——, and H. Kim, 2003: The dynamical relationship between subtropical and eddy-driven jets. *J. Atmos. Sci.,* **60,** 1490–1503.

Lindzen, R. S., and A. Y. Hou, 1988: Hadley circulations for zonally averaged heating centered off the equator. *J. Atmos. Sci.,* **45,** 2416–2427.

Lunkeit, F., K. Fraedrich, and S. E. Bauer, 1998: Storm tracks in a warmer climate: Sensitivity studies with a simplified global circulation model. *Climate Dyn.,* **14,** 813–826.

Manabe, S., and R. J. Stouffer, 1988: Two stable equilibrium of a coupled ocean–atmosphere model. *J. Climate,* **1,** 841–866.

——, J. Smagorinsky, and R. F. Strickler, 1965: Simulated climatology of a general circulation model with a hydrologic cycle. *Mon. Wea. Rev.,* **93,** 769–798.

Nakamura, H., T. Sampe, Y. Tanimoto, and A. Shimpo, 2004: Observed associations among storm tracks, jet streams, and midlatitude oceanic fronts. *Earth's Climate: The Ocean–Atmosphere Interaction.* C. Wang, S.-P. Xie, and J. A. Carton, Eds. *Geophys. Monogr.*, No. 147, Amer. Geophys. Union, 329–345.

Panetta, R. L., 1993: Zonal jets in wide baroclinically unstable regions: Persistence and scale selection. *J. Atmos. Sci.,* **50,** 2073–2106.

Pfeffer, R., 1992: A study of eddy-induced fluctuations of the zonal-mean wind using conventional and transformed Eulerian diagnostics. *J. Atmos. Sci.,* **49,** 1036–1050.

Randel, W. J., and I. M. Held, 1991: Phase speed spectra of transient eddy fluxes and critical layer absorption. *J. Atmos. Sci.,* **48,** 688–697.

Robinson, W. A., 1997: Dissipation dependence of the jet latitude. *J. Climate,* **10,** 176–182.

Schneider, E. K., 1977: Axially symmetric steady-state models of the basic state for instability and climate studies. Part II: Nonlinear calculation. *J. Atmos. Sci.,* **34,** 280–297.

Stephenson, D. B., 1995: The impact of changing the horizontal diffusion scheme on the northern winter climatology of a general circulation model. *Quart. J. Roy. Meteor. Soc.,* **121,** 211–226.

Ziegler, A. D., J. Sheffield, E. P. Maurer, B. Nijssen, E. F. Wood, and D. P. Lettenmaier, 2003: Detection of intensification in global- and continental-scale hydrological cycles: Temperature scale of evaluation. *J. Climate,* **16,** 535–547.